PNAS RESEARCH ARTICLE | MICROBIOLOGY OPEN ACCESS

Activator-induced conformational changes regulate division-associated peptidoglycan amidases

Jonathan Cook[a,1], Tyler C. Baverstock[a,1], Martin B. L. McAndrew[a], David I. Roper[a], Phillip J. Stansfeld[a], and Allister Crow[a,2]

Edited by Joe Lutkenhaus, University of Kansas Medical Center, Kansas City, KS; received February 16, 2023; accepted May 4, 2023

AmiA and AmiB are peptidoglycan-hydrolyzing enzymes from *Escherichia coli* that are required to break the peptidoglycan layer during bacterial cell division and maintain integrity of the cell envelope. In vivo, the activity of AmiA and AmiB is tightly controlled through their interactions with the membrane-bound FtsEX–EnvC complex. Activation of AmiA and AmiB requires access to a groove in the amidase-activating LytM domain of EnvC which is gated by ATP-driven conformational changes in FtsEX–EnvC complex. Here, we present a high-resolution structure of the isolated AmiA protein, confirming that it is autoinhibited in the same manner as AmiB and AmiC, and a complex of the AmiB enzymatic domain bound to the activating EnvC LytM domain. In isolation, the active site of AmiA is blocked by an autoinhibitory helix that binds directly to the catalytic zinc and fills the volume expected to accommodate peptidoglycan binding. In the complex, binding of the EnvC LytM domain induces a conformational change that displaces the amidase autoinhibitory helix and reorganizes the active site for activity. Our structures, together with complementary mutagenesis work, defines the conformational changes required to activate AmiA and/or AmiB through their interaction with their cognate activator EnvC.

bacterial cell division | X-ray crystallography | peptidoglycan | structural microbiology | Amidases

Significance

Peptidoglycan amidases break the peptidoglycan layer during cell division and maintain integrity of the cell envelope. Here, we present structures of an isolated peptidoglycan hydrolase in an autoinhibited ("off") state and a second amidase bound to the activating LytM domain of EnvC revealing the active ("on") state. A comparison of these structures provides important molecular insights into the activation of peptidoglycan hydrolases by their cognate activators.

The peptidoglycan layer is a complex molecular mesh that surrounds the bacterial cytoplasmic membrane, providing structural rigidity and protection from osmotic shock (1). In gram-negative bacteria, the peptidoglycan layer also serves as a point of attachment for the outer membrane and defines their characteristic shapes (2). During cell division, the peptidoglycan layer is broken at the division septum to allow insertion of new peptidoglycan and to separate daughter cells. In *Escherichia coli* (*E. coli*), splitting the peptidoglycan layer at the division site involves activity of three closely related periplasmic peptidoglycan amidases (3). AmiA is the smallest division-associated amidase, consisting of a simple zinc-dependent enzymatic domain of ~28 kDa. AmiB and AmiC are larger amidases (45 and 43 kDa, respectively), composed of an AmiA-like enzymatic domain and a small N-terminal domain (the "amiN" domain) that is suspected to be important in anchoring these proteins to the peptidoglycan layer (4, 5) and localization to the division site (6, 7). Both AmiA and AmiC are directed to the periplasm by the twin arginine repeat translocation (TAT) system while AmiB is exported by the Sec pathway (6, 8). A fourth amidase, AmiD, is a membrane-anchored lipoprotein that is not involved in cell division and belongs to a structurally distinct family of zinc-dependent amidases (9).

All the three division-associated amidases have overlapping enzymatic functions in hydrolyzing the peptidoglycan amide bond between the sugar and the first amino acid of the peptide cross-link (3). Single-gene knockouts of *amiA*, *amiB*, and *amiC* each have modest cell separation defects; however, strains lacking multiple amidases have severe chaining phenotypes (3). Strains lacking amidases also have increased sensitivity to antibiotics and detergents, suggesting envelope defects that allow penetration of molecules that would not usually cross the outer membrane barrier (3, 8, 10).

Because of the importance of the peptidoglycan layer for bacterial viability and cell envelope integrity, the activation of peptidoglycan amidases is carefully controlled to guard against lysis or exposure to noxious compounds in the environment. In their resting states, zinc-dependent peptidoglycan amidases such as AmiB and AmiC adopt autoinhibited conformations in which their active sites are blocked by an alpha helix containing a conserved glutamate residue which binds to the active-site zinc (5, 11). Activation of amidases is then stimulated by proteins that bind to the amidases to promote enzymatic activity (11–13). In *E. coli*, several amidase "activator" proteins (also known as murein hydrolase activators) have been identified including ActS (14, 15), EnvC (13, 16), and NlpD (13). The activators share a common motif, the LytM domain (7, 12), which forms the proposed site of amidase binding and activation (7, 17). The LytM domains of EnvC, ActS, and NlpD are also sometimes referred to as degenerate "dLytM" domains in recognition that

Author affiliations: [a]School of Life Sciences, University of Warwick, Coventry CV4 7AL, United Kingdom

Author contributions: A.C. designed research; J.C., T.C.B., M.B.L.M., and A.C. performed research; J.C. and T.C.B. contributed new reagents/analytic tools; J.C., T.C.B., M.B.L.M., P.J.S., and A.C. analyzed data; D.I.R. co-supervised T.C.B. with A.C.; P.J.S. co-supervised M.B.L.M. with A.C; and J.C., T.C.B., M.B.L.M., D.I.R., P.J.S., and A.C. wrote the paper.

The authors declare no competing interest.

This article is a PNAS Direct Submission.

[1]J.C. and T.C.B. contributed equally to this work.

[2]To whom correspondence may be addressed. Email: allister.crow@warwick.ac.uk.

This article contains supporting information online at https://www.pnas.org/lookup/suppl/doi:10.1073/pnas.2302580120/-/DCSupplemental.

Published June 5, 2023.

they lack the enzymatic activity present in the original protein from which they are named (7). Activators are themselves typically autoinhibited and are activated at specific times and places to regulate amidase activity.

One of the best understood amidase activation systems is the FtsEX–EnvC complex. FtsEX is a Type VII ABC transporter (18–20) that belongs to the same protein superfamily as MacB (19), LolCDE (21–23), BceAB (24), and HrtBA (25). During cell division, and after recruitment to the septal Z-ring (26), ATP binding and hydrolysis by FtsEX drives conformational changes in EnvC that facilitate binding and activation of AmiA and AmiB in the periplasm (17, 27). A structure of *E. coli* EnvC bound to the periplasmic domains of FtsX shows that EnvC is itself autoinhibited by the presence of a helix (the restraining arm) that blocks access to the amidase-binding groove in the EnvC LytM domain (17). Conformational change in FtsEX–EnvC is predicted to displace the restraining arm providing access for the amidase to bind the LytM domain (17); however, molecular details of how activator binding induces amidase activation remain poorly understood.

Here, we present a crystal structure of the AmiA peptidoglycan amidase in its as-isolated "resting" state and an activated form of the AmiB enzymatic domain bound to the EnvC LytM domain. Our structures show precisely how activator binding displaces the autoinhibitory helix of the amidase to allow substrate access and reorganizes the active site to promote peptidoglycan hydrolase activity.

Results

A Structure of AmiA Defines Its Active Site and Regulatory Domain. We determined a crystal structure of *E. coli* AmiA using X-ray crystallography. Crystals of AmiA diffract to a resolution of 2.4 Å and contain two molecules per asymmetric unit. Full diffraction data and refinement statistics are given in *SI Appendix*, Table S1. The secondary structure of AmiA is diagrammed in Fig. 1*A*, and a representative monomer from the structure is shown in Fig. 1*B*. As expected from its amino acid similarity, the overall fold of AmiA is very similar to previous structures of *Bartonella henselae* AmiB (11) and *E. coli* AmiC (5), including the active site (*SI Appendix*, Fig. S1). Each AmiA monomer consists of a single globular domain with a six-membered beta sheet and six alpha helices (Fig. 1 *A* and *B*). The AmiA active site is composed of a single zinc atom that is held in place by two histidine residues (His65 and His133), an aspartate (Asp135), and two glutamates (Glu80 and Glu167) (Fig. 1*C*). Similar to AmiB (11) and AmiC (5), the AmiA active-site zinc is not accessible to peptidoglycan substrates due to the presence of an alpha helix that occludes the active site; we term this feature the "blocking helix" (Fig. 1 *A* and *B*, red). As demonstrated in subsequent sections, the blocking helix has a role in autoinhibiting the activity of AmiA and forms part of a larger regulatory domain (residues 151–194) which includes a second alpha helix that constitutes the binding site for EnvC. We define the latter feature as the "interaction helix" (Fig. 1 *A* and *C*, blue). The interaction helix consists of residues 180-192 and stands conspicuously proud from the rest of the molecule. The interaction helix is also notable for possessing five solvent-facing hydrophobic residues (Leu184, Leu185, Val188, Leu189, Leu192) and is the only feature for which we identify meaningful conformational differences between the two AmiA molecules observed in the crystal structure (Fig. 1*D*). In one chain, the interaction helix is well defined, while in the other, the corresponding electron density is smeared out, consistent with thermal motion. We further assessed the dynamics of AmiA

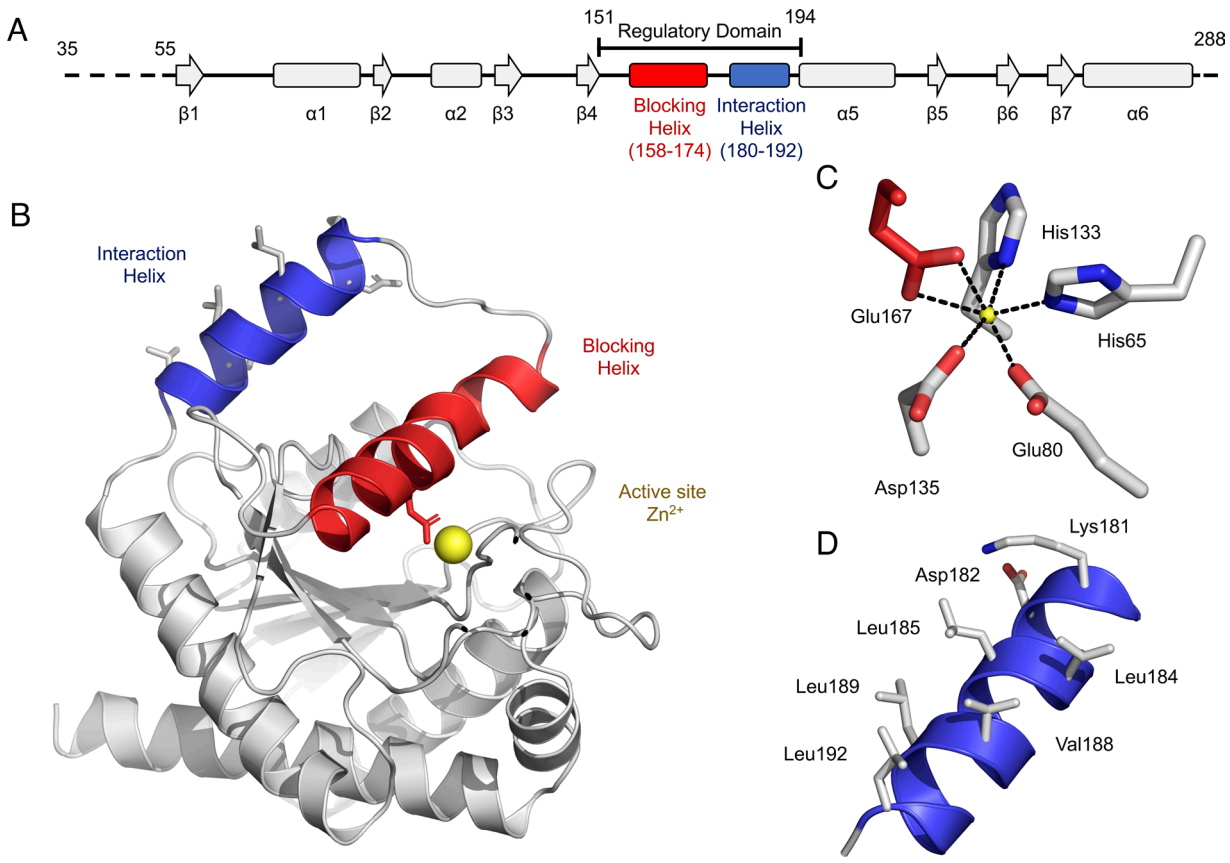

Fig. 1. Structure of *E. coli* AmiA determined by X-ray crystallography. (*A*) Secondary structure diagram for AmiA. (*B*) 3D structure of AmiA from the 2.3 Å crystal structure. (*C*) Active-site zinc and ligating residues. (*D*) Solvent-facing hydrophobic residues on the AmiA interaction helix.

by plotting the B-factors from each monomer against sequence and performing molecular dynamics simulations (*SI Appendix*, Fig. S2). Both the experimental data and simulations consistently show that the regulatory domain is much more dynamic than the rest of the protein. The overall structure of AmiA is consistent with an autoinhibited form of the enzyme in which the active-site zinc is occluded by the blocking helix, while a potential protein interaction site remains exposed to solvent ready for activation.

Mutational Analysis of the AmiA Autoinhibitory Domain. To test whether the regulatory domain maintains AmiA in an autoinhibited state, we made mutations that are predicted to relieve autoinhibition and monitored bacterial viability and detergent sensitivity when these variants were expressed in the periplasm. Expression of wild-type AmiA does not significantly disrupt viability or detergent sensitivity of *E. coli*. However, expression of AmiA variants that lack the regulatory domain causes a reduction in bacterial viability and increases bacterial sensitivity to detergent (*SI Appendix*, Fig. S3*A*). This was the case for three distinct AmiA regulatory domain deletion constructs, each engineered with different regulatory domain deletions (*SI Appendix*, Fig. S3*B*). In addition to the regulatory domain deletions, we also tested single-amino acid substitutions in Glu167 which is located on the blocking helix and, in the crystal structure, is directly ligated to the active-site zinc. The equivalent residue has previously been shown to be a key residue in maintaining autoinhibition for both AmiB (11) and AmiC (6). Mutations of Glu167 to glutamine or lysine are modestly effective in relieving AmiA autoinhibition as judged by the detergent sensitivity of strains expressing these variants in the periplasm (*SI Appendix*, Fig. S4*A*). Molecular dynamics simulations of AmiA and AmiA Glu167 mutants provide useful context to these experiments, showing that the blocking helix fluctuates between bound and free positions in the mutants, but remains locked firmly in place for the wild type (*SI Appendix*, Fig. S4 *B* and *C*). These observations are consistent with a role for the blocking helix in AmiA autoinhibition, with Glu167 forming a "latch" that anchors the blocking helix to the active-site zinc.

Mutations in the Interaction Helix Break the Interaction between AmiA and Its Activator. We next turned our attention to the function of the interaction helix. Based on the structure of AmiA, we hypothesized that the solvent-facing hydrophobic residues presented along the face of the interaction helix mediate binding to the cognate activator (EnvC). Using a bacterial 2-hybrid experiment, we assessed the interaction between AmiA and the EnvC LytM domain after introducing point mutations into the interaction helix. Wild-type AmiA binds strongly to the EnvC LytM domain, but lysine substitutions of any of the solvent-facing hydrophobics completely disrupt the interaction (Fig. 2*A*). When left for a longer period, some variants did show detectable signs of interaction—although these were significantly weaker than for the wild type consistent with partial disruption of the interaction (Fig. 2*A*). To control for the possibility that these mutations might destabilize the amidase, or differentially affect expression levels, we also ran an SDS-PAGE gel to detect the expression of each variant under identical bacterial growth conditions; all mutants were detected at the correct molecular weight with similar intensity across the gel (*SI Appendix*, Fig. S5).

To further analyze the effect of interaction helix mutations in vitro, we coexpressed a subset of AmiA variants alongside the

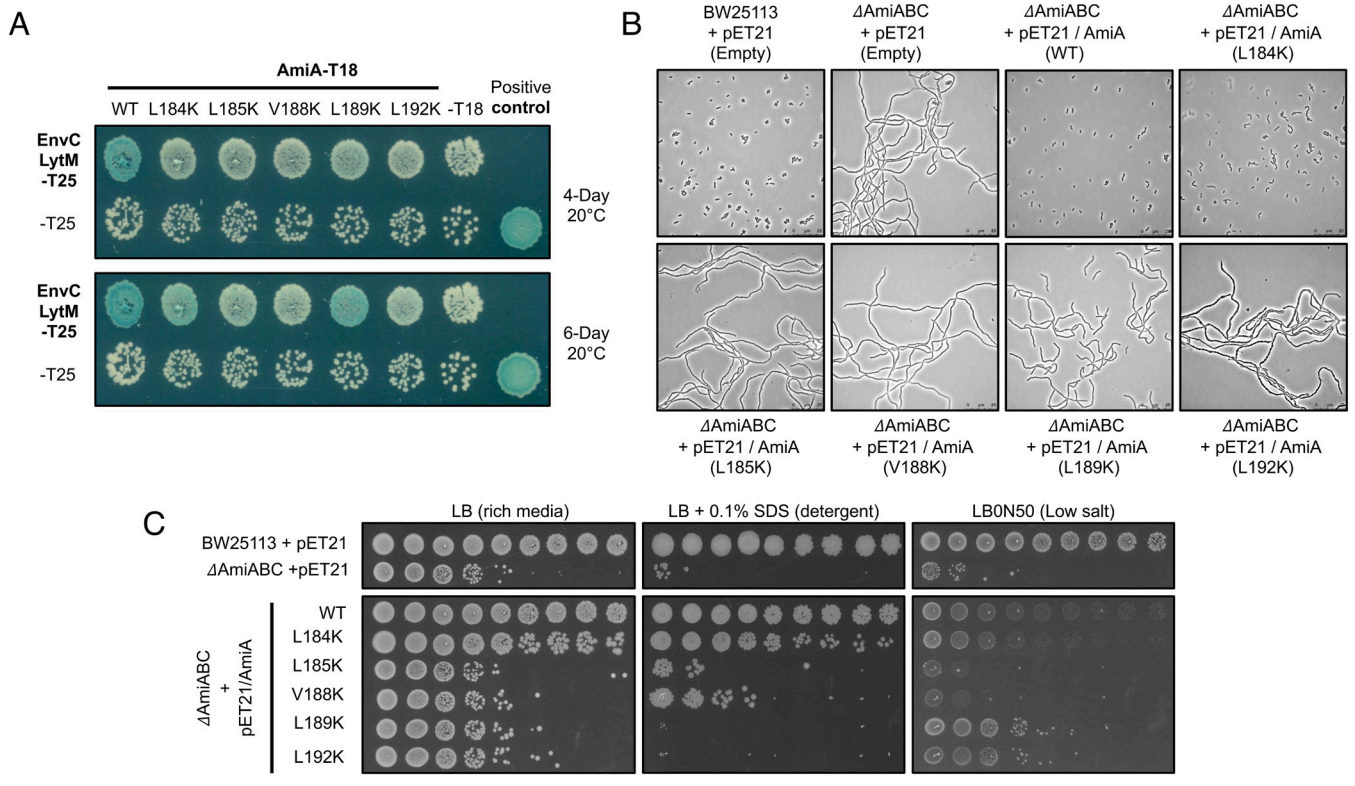

Fig. 2. Testing the importance of the AmiA interaction helix. (*A*) Bacterial 2-hybrid experiment testing the interaction between the EnvC LytM domain and AmiA for the wild-type proteins and five AmiA single amino acid variants. The top and bottom panels show the same agar plate photographed after 4 or 6 d at 20 °C. (*B*). Phase-contrast images of bacterial cultures after overnight growth. BW25113 indicates the "wild-type" *E. coli* strain and *ΔamiABC* indicates a triple-deletion knockout strain. Strains carry either an empty vector (pET21) or full-length AmiA construct (pET21/AmiA) encoding either the wild-type protein or indicated variant (*C*). Viability assays. Cultures are spotted as a series dilution, from left to right, starting with a culture adjusted to OD 1 with a 10-fold dilution at each step. LB agar reports on general viability, while SDS and LBON50 (low salt media) report on outer membrane integrity and sensitivity to osmotic challenge, respectively.

His-tagged EnvC LytM domain and assessed the stability of the complex using copurification (*SI Appendix*, Fig. S6 *A* and *B*). Consistent with the bacterial 2-hybrid data, both AmiA L184K and L185K copurify in lower yield than the wild type, and the AmiA L188K variant does not interact at all, even though all AmiA variants are highly expressed in comparison to the LytM domain (*SI Appendix*, Fig. S6*C*). We therefore conclude that the AmiA interacts with EnvC via its surface-exposed interaction helix.

Mutations in the Interaction Helix Block the Function of AmiA In Vivo. To further dissect the function of AmiA, and the role of the interaction helix, we established a multiamidase knockout strain of *E. coli* BW25113 that could be complemented by AmiA or AmiA variants (*SI Appendix*, Fig. S7). As expected from a previous triple-knockout study (3), both the cell division defect and detergent susceptibility phenotypes of the triple-amidase mutants can be corrected by expression of AmiA from a plasmid. Using this system, we tested various AmiA mutants for their ability to rescue these defects in the Δ*amiABC* background using the empty vector as a control. We used phase-contrast microscopy to inspect cells for the chaining phenotype (Fig. 2*B*), and viability on detergent agar as an indicator of cell envelope integrity (Fig. 2*C*). Four of the five AmiA variants (L185K, V188K, L189K, and L192K) and the empty vector control were highly chained and detergent sensitive, while the wild-type AmiA rescued both defects and appeared otherwise indistinguishable from the parental strain. The fifth mutant, L184K, was only modestly chained with detergent sensitivity close to wild type. These data confirm the importance of the solvent-facing residues in the interaction helix for in vivo functionality of AmiA and are consistent with roles for these residues in interactions with EnvC.

Structure of the AmiB Hydrolase Domain Bound to the Amidase-Activating EnvC LytM Domain. To better understand the molecular basis for activation of the FtsEX–EnvC-dependent amidases, we sought to determine a crystal structure of an amidase bound to its cognate LytM domain. Our strategy was to identify well-expressed and stable amidase activator pairs and screen for crystallization using robotics. Using copurification experiments, we first demonstrated that AmiA could be successfully purified with isolated LytM domain of EnvC (*SI Appendix*, Fig. S8). We also showed that AmiA does not copurify with either the full-length EnvC protein or an EnvC construct lacking the coiled coil, consistent with EnvC being autoinhibited by the presence of the EnvC restraining arm in these constructs. These experiments complement previous work showing copurification of the EnvC periplasmic domain with AmiB, and bacterial 2-hybrid assays confirming this pattern of interactions for AmiA and AmiB in *E. coli* (17). The experiment also confirms that the same autoinhibition mechanism that regulates EnvC's activation of AmiB applies to AmiA.

Screening activator/amidase pairs from multiple organisms, we identified several well-expressed amidase hydrolytic domains that copurified with their cognate EnvC LytM domains. This included both AmiA and AmiB constructs, the latter of which were cloned without their N-terminal "AmiN" domain. After extensive crystallization trials, we were ultimately successful in solving a crystal structure of the AmiB hydrolytic domain bound to the EnvC LytM domain using proteins from *Citrobacter rodentium*.

The 3.4 Å structure of the AmiB hydrolytic domain bound to the EnvC LytM domain is shown in Fig. 3. Inspecting the architecture of the complex (Fig. 3*A*), three observations are immediately apparent. First, the EnvC LytM domain is bound directly to the amidase interaction helix, with the latter's hydrophobic residues all pointing directly into the LytM groove (Fig. 3*B*). Second, the amidase regulatory domain has a very different conformation in the EnvC-bound structure such that the interaction helix is contiguous with helix 5 and the blocking helix is displaced from the active site (Fig. 3*A*). Finally, the active-site zinc is ligated by three residues rather than the five (Fig. 3*C*) due to the absence of the blocking helix glutamate (Glu167 in AmiA) and dissociation of one of the aspartates (Asp271 in AmiB, equivalent to Asp135 in AmiA). An alignment of AmiA and AmiB regulatory domain sequences is provided in Fig. 3*D* to assist the reader in matching equivalent residues. The structure confirms the predicted importance of the surface-facing hydrophobic residues along the interaction helix and confirms binding-induced conformational change as a mechanism for amidase activation.

The Amidase's Interaction Helix Binds in the Same Groove as the EnvC Restraining Arm. In a crystal structure of full-length EnvC bound to the two periplasmic domains of FtsX, it was noted that the LytM domain is occupied by a long helix (the "restraining arm") that blocks access to the amidase-binding groove (17). This led to the proposal that the restraining arm would need to be displaced by a conformational change to allow amidase to bind and be activated. The conformational change is expected to be driven by ATP binding and hydrolysis by FtsEX and propagated through the coiled coil of EnvC. The structure of the EnvC–LytM AmiB complex shows that the amidase interaction helix binds within the same groove as the restraining arm, lending further support for this mechanism (Fig. 4 *A* and *B*).

The interface of the AmiB–EnvC complex is governed by interactions between the exterior hydrophobic residues of the amidase and residues lining the interior of the EnvC LytM groove. Consistent with the structure, several contact residues inside the LytM groove have previously been identified as important for amidase activation in *E. coli* EnvC (7). Additionally, the activator–amidase structure further identifies a distinctive loop (*C. rodentium* EnvC residues G319–G330) that contacts residues located *between* the interaction helix and helix 5. The extended loop wraps around the residues located between the interaction helix and helix 5, causing them to form a single, continuous, helical element (Fig. 4*B*). Taken together, the two amidase structures capture a significant conformational change in the regulatory domain as the N-terminal end of interaction helix is prised away from the enzymatic domain by the binding of EnvC. The knock-on effect of this levering motion is to pull the sequence-neighboring blocking helix away from the zinc exposing the active site for peptidoglycan binding.

Reorganization of the Activated Zinc Site in the EnvC-Bound Amidase. In addition to the dislocation of the blocking helix, which is tied to dissociation of Glu167/Glu303 from the active-site zinc, we also observed displacement of Asp135/Asp271 (Fig. 3*C*). Consequently, the amidase zinc site is surrounded by five residues in the resting state (Fig. 1*C*) but only three in the activated (EnvC LytM bound) state (Fig. 3*C*). In the EnvC LytM AmiB costructure, the angles between neighboring ligating residues and the zinc are all close to 109°, suggesting a tetrahedral coordination state in which the fourth position remains open for substrate binding and catalysis.

Inspecting the density surrounding the zinc, a low-occupancy ligand is present at the fourth position of the coordination sphere. The ligand is consistent with a sugar molecule in chair conformation (*SI Appendix*, Fig. S9). No sugars were used in crystallizing the complex and thus this molecule seems to have been copurified during protein production. The sugar could be a product of

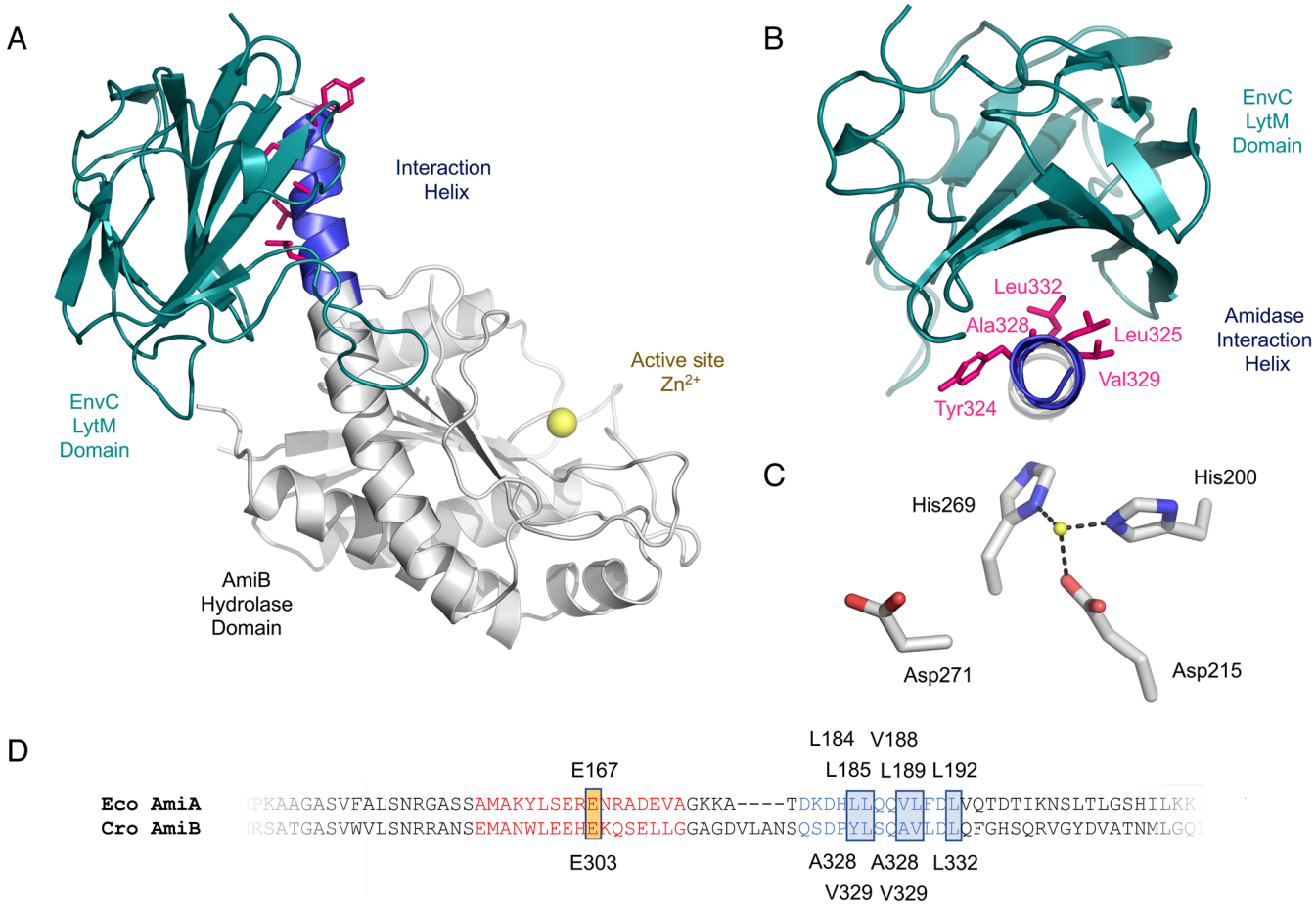

Fig. 3. Structure of the amidase–activator complex. (*A*) 3.4 Å crystal structure of the AmiB enzymatic domain from *C. rodentium* bound to the cognate LytM activation domain of EnvC. (*B*) Close-up view of AmiB–EnvC–LytM interface. (*C*) Close-up of the active-site ligands in the AmiB–EnvC–LytM complex. (*D*) Sequence alignment between *E. coli* AmiA and *C. rodentium* AmiB centered over the regulatory domain. Amino acids corresponding to the blocking helix and interaction helix are shown in red and blue, respectively. Key residues are highlighted to assist identification of functionally equivalent residues.

peptidoglycan hydrolysis; however, due to modest resolution (3.4 Å) and partial occupancy, we have not yet formally identified this molecule. We anticipate that future high-resolution studies may be able to resolve this ligand, and perhaps characterize further natural substrates, reaction products, or even inhibitors, bound to the amidase.

Discussion

Peptidoglycan amidases are key hydrolytic enzymes that are needed to break the peptidoglycan layer during cell division to allow for separation of daughter cells. Here, we described two crystal structures that capture both the active and inactive states of the amidase, showing precisely how division-associated peptidoglycan hydrolases are activated by their interaction with a cognate partner, EnvC. We first described the crystal structure of an isolated *E. coli* amidase, AmiA, at 2.4 Å resolution. The structure reveals an inactive form of the enzyme where the active-site zinc is blocked by an autoinhibitory helix, with a solvent-facing helix that forms the binding site for its cognate activator (Fig. 1). We then showed the importance of the interaction helix using site-directed mutagenesis. Mutations in the interaction helix disrupt interaction with EnvC and prevent activation of the amidase in vivo (Fig. 2). A structure of AmiB bound to the EnvC LytM domain further establishes the interaction helix as the EnvC-binding site and reveals the activation mechanism; the amidase interaction helix docks inside of an EnvC surface groove, forcing conformational changes in the neighboring autoinhibitory helix that expose the active site (Fig. 3). Displacement of the blocking helix not only makes the active site accessible to substrates, but also reconfigures the ligands surrounding the active-site zinc. Finally, we show that the groove in the LytM domain of EnvC that forms the amidase-binding site is the same groove that is blocked by the EnvC restraining arm (Fig. 4). The structures show that autoinhibition is a feature of both the amidase and the activator, and that the interaction between the activator and amidase involves substantial conformational changes.

An updated mechanism for amidase activation in the FtsEX–EnvC–AmiA system is presented in Fig. 5. During periods of inactivity, both the amidase and the FtsEX–EnvC complex are autoinhibited (Fig. 5, *Top Left*): AmiA is autoinhibited by its blocking helix which prevents the binding of peptidoglycan and the FtsEX–EnvC complex is autoinhibited by the restraining arm which prevents recruitment of the amidase to the LytM domain. Upon ATP binding to FtsEX–EnvC, a long-range conformational change is transmitted through EnvC, freeing the LytM domain from the restraining arm and exposing the amidase-binding site (Fig. 5, *Top Right*). Binding of the amidase to the EnvC LytM domain relies upon the amidase interaction helix, which binds in the same location from which the restraining arm was displaced (Fig. 5, *Bottom*). Upon binding, the amidase undergoes an induced conformational change in which the blocking helix is displaced from the active site. Rearrangement of the ligands surrounding the active-site zinc leads to peptidoglycan amidase activity. Finally,

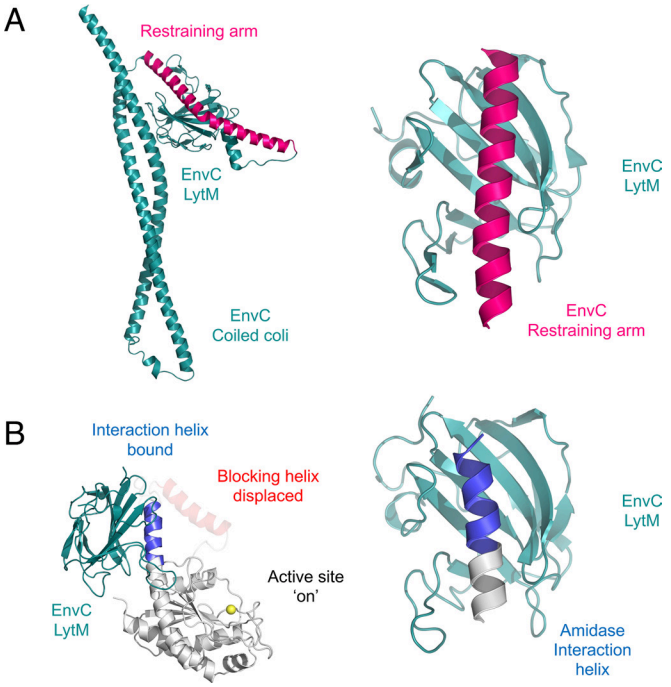

Fig. 4. The amidase interaction helix binds in the same groove as the EnvC restraining arm. (*A*) Structure of EnvC showing the autoinhibitory restraining arm (*pink*) bound within its LytM domain (*teal*). A close-up view is shown to the right. (*B*) Structure of the activated amidase bound by the activating EnvC LytM domain. The displaced blocking helix (*red*) was too disordered to build in the crystal structure of the complex (most likely due to high mobility), but is shown here in a semi-transparent form to indicate a feasible position given the observed location of the (well ordered) interaction helix (*blue*). A close-up view of the amidase interaction helix bound in the LytM groove is shown to the right for comparison with the restraining-arm-bound LytM domain immediately above.

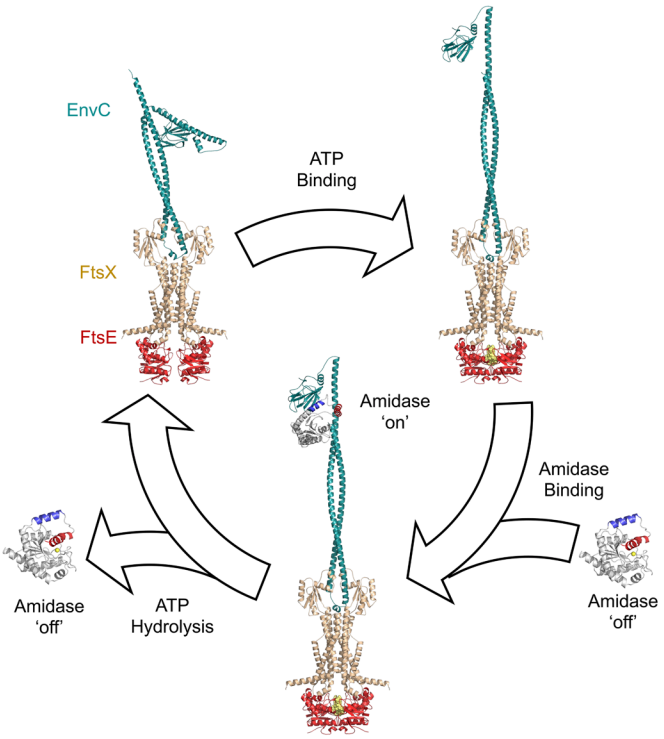

Fig. 5. Mechanism of amidase activation by FtsEX–EnvC. Full details are given in the *Discussion*. Theoretical models are constructed using a combination of Alphafold predictions (28, 29) and experimentally determined crystal structures [6TPI (17), 8C2O, and 8C0J].

ATP hydrolysis allows the system to reset; the amidase is released and EnvC restraining arm returns to the LytM groove (Fig. 5, *Top Left*). A near-identical mechanism likely operates for FtsEX–EnvC–AmiB, although in that case the amidase may additionally be prelocated at the division site by interactions between the N-terminal "AmiN" domain and the peptidoglycan layer (4–7). For AmiA, which lacks an AmiN domain, localization to the division site most likely relies on interactions between FtsEX–EnvC or other components of the division machinery. A key feature of this proposed mechanism is that the amidase is only briefly activated since the eventual hydrolysis of ATP by FtsEX returns the complex to the inactive autoinhibited state. Once the amidase is released, it is rapidly autoinhibited by the blocking helix returning to the peptidoglycan binding groove.

LytM domains are widespread among amidase activators (12), with predicted LytM domains in both NlpD (30) (the activator for AmiC) and ActS (12, 14) (formerly known as YgeR—an activator of AmiC, AmiA, and AmiB) of *E. coli*. The interaction described here for EnvC and its cognate amidases (AmiA and AmiB) may well serve as a useful model for understanding these interactions.

The apparent redundancy between division-associated amidases and the large number of murein hydrolase activators raises the question of why such complexity is required. This is especially true for the FtsEX–EnvC–AmiA/AmiB system since the gram-positive equivalent, FtsEX–PcsB, operates without separate amidases and instead uses an EnvC-like protein (PcsB) that has its own peptidoglycan hydrolase activity (31, 32). Maintaining amidases in several different parts of the gram-negative cell envelope may be advantageous for separating the peptidoglycan layer while coordinating invagination of the outer membrane, as suggested for NlpD–AmiC (30). Overlapping specificity of amidases and activators may be useful under different environmental stress conditions as has been suggested for ActS (33).

In summary, we have determined the structures of two peptidoglycan amidases (AmiA and AmiB) in autoinhibited and activated states and relate these to their wider regulation through interactions with a cognate activator, the LytM domain of FtsEX–EnvC. The structures reveal near-atomic details of the conformational changes in the amidase that are required for activation of peptidoglycan hydrolysis including displacement of the autoinhibitory helix, and rearrangement of the sidechains that surround the active-site zinc. Our data significantly advance our understanding of a key event in bacterial cell division (breakage of the peptidoglycan layer) and provide fascinating molecular insights into the conformational changes that regulate amidase activity.

Methods

A full set of methods are given in *SI Appendix*. In brief, structures of AmiA and the complex between the AmiB enzymatic domain and the EnvC LytM domain were determined using X-ray crystallography using software from CCP4 suite (34) with molecular replacement probes generated by Alphafold (28, 29). Coordinates and structure factors have been deposited with the protein data bank (accession codes **8C20** and **8C0J**). Bacterial viability and detergent susceptibility were assessed by spotting out bacterial cultures in 10-fold series dilution on LB agar or LB agar supplemented with 0.1 % (w/v) SDS. All strains carry a plasmid providing ampicillin resistance as a selection marker and agar was supplemented with 50 μg/mL ampicillin and 1 mM IPTG. MICs were determined in microbroth culture using LB containing 50 μg/mL ampicillin and 1 mM IPTG. Bacterial 2-hybrid experiments used the BACTH system (35). The wild-type *E. coli* BW25113 and single-amidase knockout strains were obtained from the Keio collection (36). The double- and triple-amidase knockout strains were produced in the same background using

Genebridges gene deletion kit (37). Phase-contrast microscopy was performed after overnight growth in LB containing 1mM IPTG and 50 μg/mL ampicillin. Molecular dynamics simulations used Gromacs (38) with the Charm forcefield (39). Structural figures were produced with Pymol (40).

Data, Materials, and Software Availability. Crystal structure coordinates and structure factors data have been deposited in Protein Data Bank (8C2O (41) is the structure of *E. coli* AmiA and 8C0J (42) is the structure of the AmiB enzymatic domain bound to the EnvC LytM domain.

ACKNOWLEDGMENTS. This work was funded by BBSRC New Investigator award to A.C. (BB/V017101/1) and supported by BB/N003241/1 to D.I.R. Research in P.J.S.'s lab is funded by Wellcome (208361/Z/17/Z), the MRC (MR/S009213/1), BBSRC (BB/P01948X/1, BB/R002517/1, and BB/S003339/1), and the Howard Dalton Centre. We also thank the BBSRC and Medical Research Council for funding PhD work by T.C.B. (BB/M01116X/1) and M.B.L.M. (MR/N014294/1); staff at Diamond Synchrotron for use of X-ray data collection facilities; Prof. Nick Waterfield for use of a phase-contrast microscope; Warwick School of Life Sciences media kitchen for providing bacterial growth media; and Warwick Technicians for technical support.

1. W. Vollmer, D. Blanot, M. A. De Pedro, Peptidoglycan structure and architecture. *FEMS Microbiol. Rev.* **32**, 149–167 (2008).
2. T. J. Silhavy, D. Kahne, S. Walker, The bacterial cell envelope. *Cold Spring Harb. Perspect. Biol.* **2**, a000414 (2010).
3. C. Heidrich *et al.*, Involvement of N-acetylmuramyl-l-alanine amidases in cell separation and antibiotic-induced autolysis of Escherichia coli: Cell separation and antibiotic-induced autolysis of E. coli. *Mol. Microbiol.* **41**, 167–178 (2001).
4. R. F. de Souza, V. Anantharaman, S. J. de Souza, L. Aravind, F. J. Gueiros-Filho, AMIN domains have a predicted role in localization of diverse periplasmic protein complexes. *Bioinformatics* **24**, 2423–2426 (2008).
5. M. Rocaboy *et al.*, The crystal structure of the cell division amidase AmiC reveals the fold of the AMIN domain, a new peptidoglycan binding domain: Crystal structure of AmiC of *Escherichia coli*. *Mol. Microbiol. 90*, 267–277 (2013).
6. T. G. Bernhardt, P. A. J. De Boer, The Escherichia coli amidase AmiC is a periplasmic septal ring component exported via the twin-arginine transport pathway: Amidase transport and localization. *Mol. Microbiol.* **48**, 1171–1182 (2003).
7. N. T. Peters *et al.*, Structure-function analysis of the LytM domain of EnvC, an activator of cell wall remodelling at the *Escherichia coli* division site: EnvC LytM domain structure. *Mol. Microbiol.* **89**, 690–701 (2013).
8. B. Ize, N. R. Stanley, G. Buchanan, T. Palmer, Role of the Escherichia coli Tat pathway in outer membrane integrity: AmiA and AmiC are Tat substrates. *Mol. Microbiol.* **48**, 1183–1193 (2003).
9. F. Kerff *et al.*, Specific structural features of the N-acetylmuramoyl-L-alanine amidase AmiD from Escherichia coli and mechanistic implications for enzymes of this family. *J. Mol. Biol.* **397**, 249–259 (2010).
10. A. A. Yakhnina, H. R. McManus, T. G. Bernhardt, The cell wall amidase AmiB is essential for *P seudomonas aeruginosa* cell division, drug resistance and viability: *Pseudomonas* amidases. *Mol. Microbiol.* **97**, 957–973 (2015).
11. D. C. Yang, K. Tan, A. Joachimiak, T. G. Bernhardt, A conformational switch controls cell wall-remodelling enzymes required for bacterial cell division: Control of cell wall-remodelling enzymes. *Mol. Microbiol.* **85**, 768–781 (2012).
12. T. Uehara, T. Dinh, T. G. Bernhardt, LytM-domain factors are required for daughter cell separation and rapid ampicillin-induced lysis in *Escherichia coli*. *J. Bacteriol.* **191**, 5094–5107 (2009).
13. T. Uehara, K. R. Parzych, T. Dinh, T. G. Bernhardt, Daughter cell separation is controlled by cytokinetic ring-activated cell wall hydrolysis. *EMBO J.* **29**, 1412–1422 (2010).
14. C. K. Gurnani Serrano *et al.*, ActS activates peptidoglycan amidases during outer membrane stress in *Escherichia coli*. *Mol. Microbiol.* **116**, 329–342 (2021).
15. P. K. Chodisetti, R. Bahadur, R. N. Amrutha, M. Reddy, A LytM-domain factor, ActS, functions in two distinctive peptidoglycan hydrolytic pathways in E. coli. *Front. Microbiol.* **13**, 913949 (2022).
16. H. Hara *et al.*, Identification and characterization of the *Escherichia coli envC* gene encoding a periplasmic coiled-coil protein with putative peptidase activity. *FEMS Microbiol. Lett.* **212**, 229–236 (2002).
17. J. Cook *et al.*, Insights into bacterial cell division from a structure of EnvC bound to the FtsX periplasmic domain. *Proc. Natl. Acad. Sci. U.S.A.* **117**, 28355–28365 (2020).
18. C. Thomas *et al.*, Structural and functional diversity calls for a new classification of ABC transporters. *FEBS Lett.* **594**, 3767–3775 (2020).
19. A. Crow, N. P. Greene, E. Kaplan, V. Koronakis, Structure and mechanotransmission mechanism of the MacB ABC transporter superfamily. *Proc. Natl. Acad. Sci. U.S.A.* **114**, 12572–12577 (2017).
20. N. P. Greene, E. Kaplan, A. Crow, V. Koronakis, Antibiotic resistance mediated by the MacB ABC transporter family: A structural and functional perspective. *Front. Microbiol.* **9**, 950 (2018).
21. E. Kaplan, N. P. Greene, A. Crow, V. Koronakis, Insights into bacterial lipoprotein trafficking from a structure of LolA bound to the LolC periplasmic domain. *Proc. Natl. Acad. Sci. U.S.A.* **115**, E7389–E7397 (2018).
22. S. Sharma *et al.*, Mechanism of LolCDE as a molecular extruder of bacterial triacylated lipoproteins. *Nat. Commun.* **12**, 4687 (2021).
23. W. Bei *et al.*, Cryo-EM structures of LolCDE reveal the molecular mechanism of bacterial lipoprotein sorting in Escherichia coli. *PLoS Biol.* **20**, e3001823 (2022).
24. N. L. George, A. L. Schilmiller, B. J. Orlando, Conformational snapshots of the bacitracin sensing and resistance transporter BceAB. *Proc. Natl. Acad. Sci. U.S.A.* **119**, e2123268119 (2022).
25. H. Nakamura *et al.*, Structural basis for heme detoxification by an ATP-binding cassette–type efflux pump in gram-positive pathogenic bacteria. *Proc. Natl. Acad. Sci. U.S.A.* **119**, e2123385119 (2022).
26. S. Du, W. Henke, S. Pichoff, J. Lutkenhaus, How FtsEX localizes to the Z ring and interacts with FtsA to regulate cell division. *Mol. Microbiol.* **112**, 881–895 (2019).
27. D. C. Yang *et al.*, An ATP-binding cassette transporter-like complex governs cell-wall hydrolysis at the bacterial cytokinetic ring. *Proc. Natl. Acad. Sci. U.S.A.* **108**, E1052–E1060 (2011).
28. J. Jumper *et al.*, Highly accurate protein structure prediction with AlphaFold. *Nature* **596**, 583–589 (2021).
29. M. Mirdita *et al.*, ColabFold: Making protein folding accessible to all. *Nat. Methods* **19**, 679–682 (2022).
30. M.-J. Tsang, A. A. Yakhnina, T. G. Bernhardt, NlpD links cell wall remodeling and outer membrane invagination during cytokinesis in Escherichia coli. *PLoS Genet* **13**, e1006888 (2017).
31. L.-T. Sham, S. M. Barendt, K. E. Kopecky, M. E. Winkler, Essential PcsB putative peptidoglycan hydrolase interacts with the essential $FtsX_{Spn}$ cell division protein in *Streptococcus pneumoniae* D39. *Proc. Natl. Acad. Sci. U.S.A.* **108**, E1061–E1069 (2011).
32. S. G. Bartual *et al.*, Structural basis of PcsB-mediated cell separation in Streptococcus pneumoniae. *Nat. Commun.* **5**, 3842 (2014).
33. E. A. Mueller *et al.*, The active repertoire of *Escherichia coli* peptidoglycan amidases varies with physiochemical environment. *Mol. Microbiol.* **116**, 311–328 (2021).
34. M. D. Winn *et al.*, Overview of the *CCP* 4 suite and current developments. *Acta Crystallogr. D Biol. Crystallogr.* **67**, 235–242 (2011).
35. G. Karimova, J. Pidoux, A. Ullmann, D. Ladant, A bacterial two-hybrid system based on a reconstituted signal transduction pathway. *Proc. Natl. Acad. Sci. U.S.A.* **95**, 5752–5756 (1998).
36. T. Baba *et al.*, Construction of *Escherichia coli* K-12 in-frame, single-gene knockout mutants: The Keio collection. *Mol. Syst. Biol.* **2**, 2006.0008 (2006).
37. Y. Zhang, F. Buchholz, J. P. P. Muyrers, A. F. Stewart, A new logic for DNA engineering using recombination in Escherichia coli. *Nat. Genet* **20**, 123–128 (1998).
38. M. J. Abraham *et al.*, GROMACS: High performance molecular simulations through multi-level parallelism from laptops to supercomputers. *SoftwareX* **1–2**, 19–25 (2015).
39. J. Huang *et al.*, CHARMM36m: An improved force field for folded and intrinsically disordered proteins. *Nat. Methods* **14**, 71–73 (2017).
40. L. L. C. Schrödinger, The PyMOL Molecular Graphics System (Version 1.8, 2015).
41. T. C. Baverstock, A. Crow, Structure of E. coli AmiA. Protein Data Bank. https://www.rcsb.org/structure/8C2O. Deposited 22 December 2022.
42. A. Crow, Structure of AmiB enzymatic domain bound to the EnvC LytM domain. Protein Data Bank. https://www.rcsb.org/structure/8C0J. Deposited 17 December 2022.

Supplemental Information

Activator-induced conformational changes regulate division-associated peptidoglycan amidases

Jonathan Cook†, Tyler C. Baverstock†, Martin B.L. McAndrew, David I. Roper, Phillip J. Stansfeld, Allister Crow*

Schedule of Supplemental Information

Table S1: Data collection and refinement statistics

	AmiA 8C2O	EnvC-LytM:AmiB Complex 8C0J
Data collection		
Beam line	Diamond I04-1	Diamond I04
Wavelength (Å)	0.97950	0.95373
Crystal parameters		
Space group	P 2 2_1 2_1	I 4_1 3 2
Unit cell dimensions (Å)	59.5, 73.9, 115.6	237.4, 237.4, 237.4
Unit cell angles (°)	90, 90, 90	90, 90, 90
Reflection data[*]		
Resolution range (Å)	59.51-2.35 (2.43-2.35)	59.34-3.38 (3.65-3.38)
Unique reflections	21,955 (2,121)	16,294 (3,305)
R_{pim}	0.050 (0.506)	0.088 (0.686)
I/σ(I)	10.4 (1.5)	9.9 (1.6)
$CC_{½}$	0.999 (0.662)	0.998 (0.939)
Completeness (%)	100 (100)	100 (100)
Multiplicity	12.6 (12.1)	78.2 (78.9)
Wilson B ($Å^2$)	51	81
Refinement[†]		
Resolution (Å)	59.60 - 2.35	50.00 - 3.38
Number of reflections	20,819	15,286
$R_{overall}$	0.177	0.249
R_{free}	0.236	0.291
Rms (bond lengths) (Å)	0.007	0.008
Rms (bond angles) (°)	1.43	1.41
Model B-factors		
Proteins ($Å^2$)	50, 60	110, 123, 142
Zn ($Å^2$)	42, 43	95, 139
Waters ($Å^2$)	43	-
Ramachandran statistics[‡]		
Favoured (%)	97.6	91.9
Allowed (%)	2.4	7.9
Outlier (%)	0	0.2

Values in parentheses indicate the highest resolution bin.
Refinement statistics are from Refmac.
Ramachandran statistics as reported by Rampage.

Table S2: Plasmids used in this study.

Plasmid	Vector type	Contents	Tag	Figure
pTB1 034	pET21a	sol AmiA (35-289)	C term HIS	1
pTB1 022	pETDuet-1	EnvC (35-419) plus AmiA (35-289)	N term HIS	S8
pTB1 023	pETDuet-1	EnvC (222-419) plus AmiA (35-289)	N term HIS	S8
pTB1 016 *	pETDuet-1	EnvC (277-419) plus AmiA (35-289)	N term HIS on EnvC (277-419)	S8, S6
pCRoAmiBenzEnvCact	pETDuet-1	Citrobacter LytM (284-420) plus enzAmiB (190-442)	N term HIS	3
pTB1 028	pET21a	full AmiA	no tag	S3, S4, S5
pTB1 029	pET21a	full AmiB	no tag	S5
pTB1 030	pET21a	full AmiC	no tag	S5
pTB1 050	pET21a	full AmiA Δreg-1	no tag	S3
pTB1 055	pET21a	full AmiA Δreg-2	no tag	S3
pTB1 056	pET21a	full AmiA Δ-reg-3	no tag	S3
pTB1 011 *	pUT18C	sol AmiA (35-289) wt	-T18	2, S4
pJC6 622	pUT18C	sol AmiA L184K	-T18	2, S4
pJC6 624	pUT18C	sol AmiA L185K	-T18	2, S4
pJC6 627	pUT18C	sol AmiA V188K	-T18	2, S4
pJC6 629	pUT18C	sol AmiA L189K	-T18	2, S4
pJC6 645	pUT18C	sol AmiA L192K	-T18	2, S4
pJC6 257 *	pK N T25	EnvC LytM (278-419)	-T25	2, S4
pJC6 620	pUC	full AmiA		
pJC6 659	pUC	full AmiA E167K		
pJC6 698	pUC	full AmiA E167Q		
pJC6 882	pUC	full AmiA L184K		
pJC6 885	pUC	full AmiA L185K		
pJC6 888	pUC	full AmiA V188K		
pJC6 893	pUC	full AmiA L189K		

pJC6 894	pUC	full AmiA L192K		
pJC6 689	pET21a	full AmiA E167K	no tag	S4
pJC6 709	pET21a	full AmiA E167Q	no tag	S4
pJC6 898	pET21a	full AmiA L184K	no tag	S4
pJC6 899	pET21a	full AmiA L185K	no tag	S4
pJC6 901	pET21a	full AmiA V188K	no tag	S4
pJC6 908	pET21a	full AmiA L189K	no tag	S4
pJC6 909	pET21a	full AmiA L192K	no tag	S4
pJC7 054	pETDuet-1	EnvC (277-419) plus AmiA (35-289) (L184K)	N-term His-tag on EnvC (277-419)	S6
pJC7 056	pETDuet-1	EnvC (277-419) plus AmiA (35-289) (L185K)	N-term His-tag on EnvC (277-419)	S6
pJC7 058	pETDuet-1	EnvC (277-419) plus AmiA (35-289) (L188K)	N-term His-tag on EnvC (277-419)	S6

* Indicated vectors from Cook et al 2020 (1).

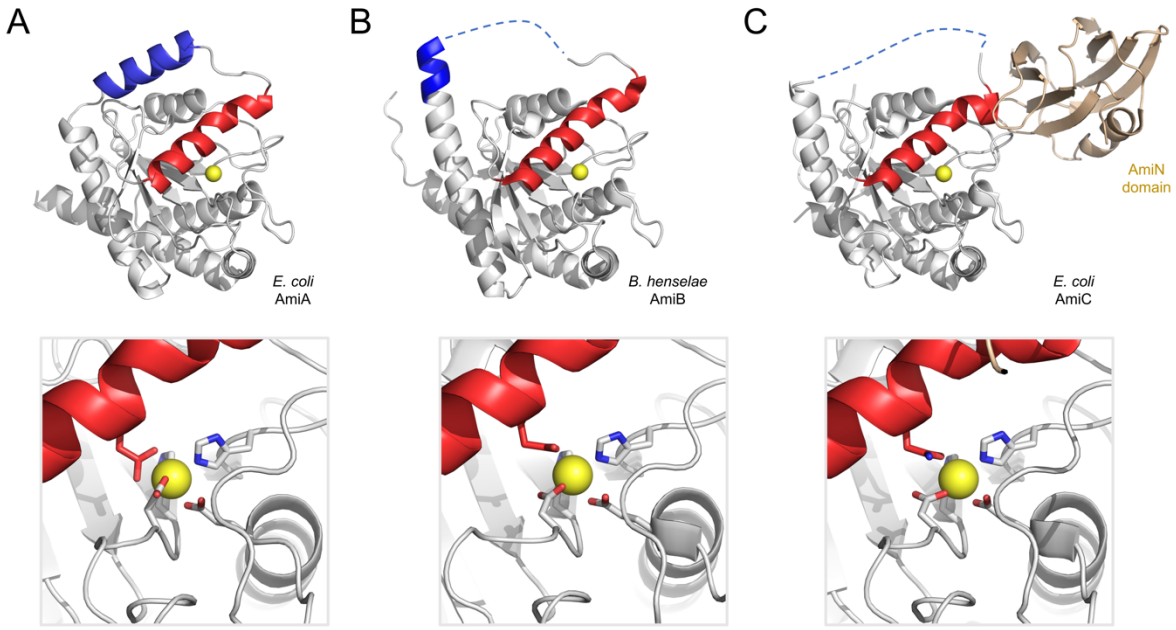

Figure S1: Comparison of *E. coli* AmiA with structures of *Bartonella henselae* AmiB and *E. coli* AmiC. (A) Structure *E. coli* AmiA presented here (pdb entry 8C2O). Red indicates the autoinhibitory blocking helix and interaction helix in blue. The other structures are coloured similarly. (B) Structure of AmiB from *Bartonella henselae* (2) (3NE8 chain A). The N-terminal domain is not present. (C) Structure of *E. coli* AmiC (3) (4BIN chain A). A short linker between the AmiN domain and the enzymatic domain (residues 152-162) is hidden for clarity. Close-up views of the zinc active site are shown below the structures. An unmodelled loop in both AmiB and AmiC is shown as a dotted line. Enzymatic domains of AmiB and AmiC can be superposed on AmiA with RMSD values of 0.76 Å and 0.51 Å respectively.

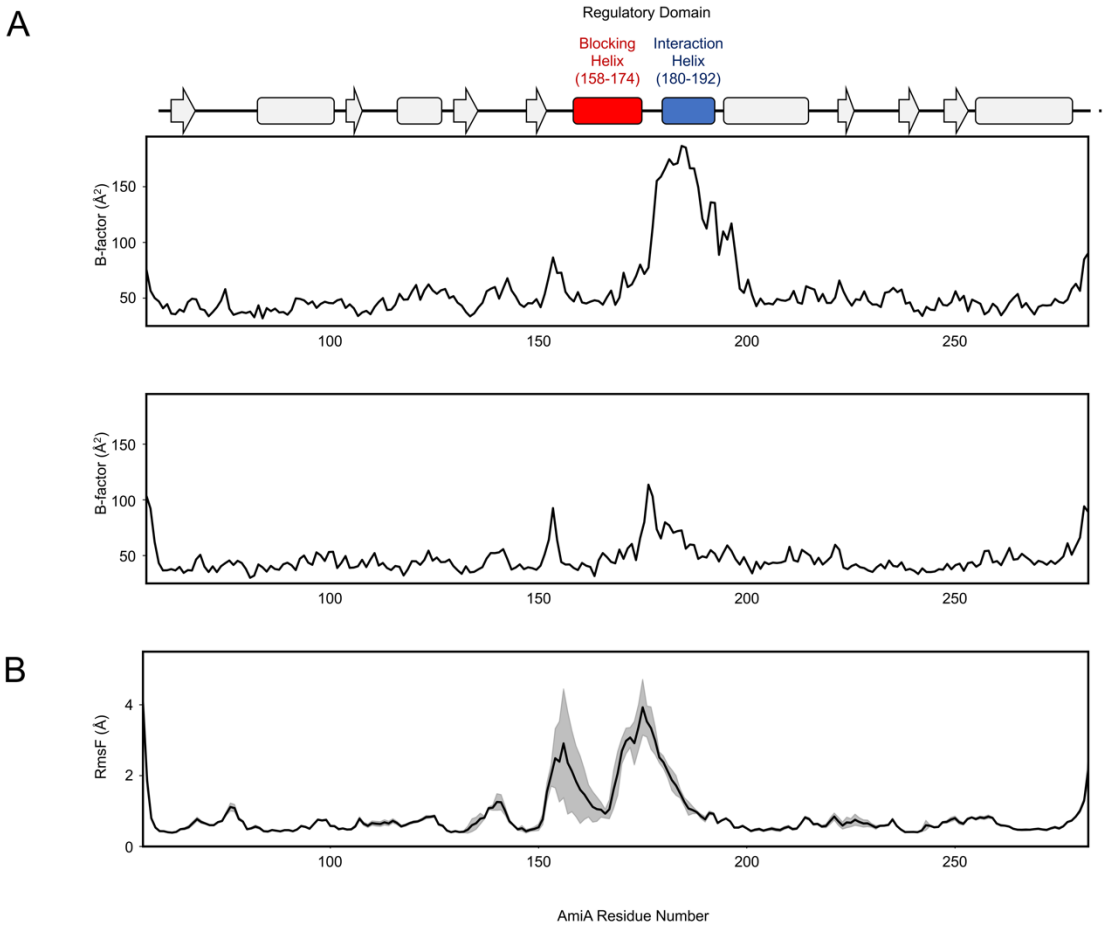

Figure S2: Flexibility in AmiA. (**A**) B-factor plots for AmiA showing high mobility in the Regulatory domain. (**B**) Plot of RmsF (Root-mean-square Fluctuations) over the course of a 500 ns simulation of AmiA.

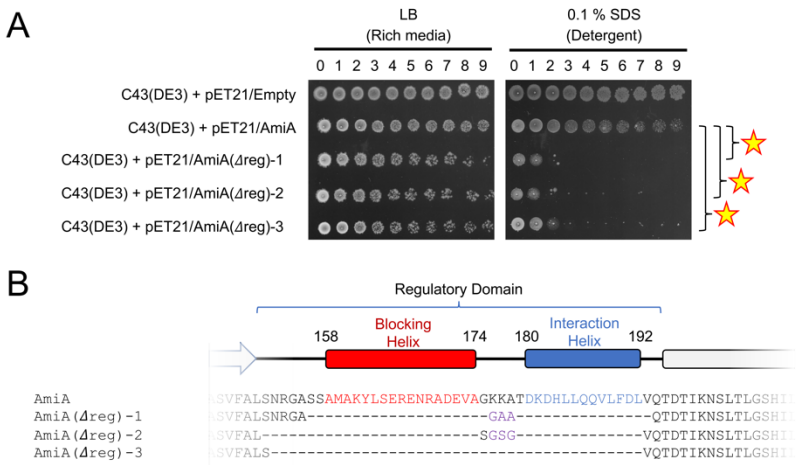

Figure S3: Overexpression of AmiA constructs lacking their regulatory domains causes an outer membrane defect in *E. coli*. (**A**) Viability assays for *E. coli* C43(DE3) carrying either an empty vector, wild type AmiA, or one of three AmiA constructs lacking the regulatory domain. Stars indicate significant differences in detergent sensitivity. (**B**) Amino acid sequence alignment for AmiA and three constructs engineered to lack the regulatory domain. The three constructs differ in the design of the linker replacing the regulatory domain deletion.

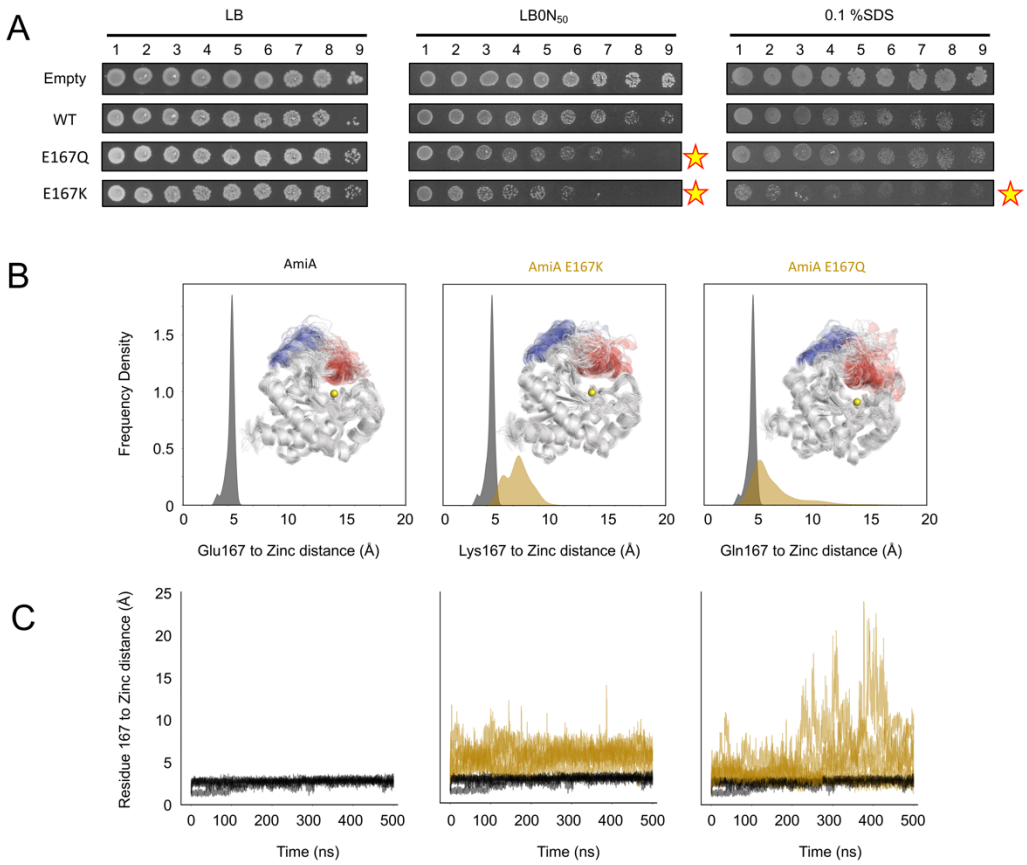

Figure S4: Mutational analysis of AmiA Glu167. (**A**) Viability assays for *E. coli* expressing either wild type AmiA or the indicated Glu167 variant (E167Q, E167K). Cultures were adjusted to OD600 =1 and series diluted using 10-fold steps. Cells were then spotted on LB, LB0N50 or 0.1 % SDS to test viability, osmotic sensitivity and detergent sensitiviy. (**B**) Histograms showing the distribution of distances between the Glu167 C-alpha atom and the active site zinc over the course of five 500 ns simulations of AmiA, AmiA E167Q and E167K. Structural ensembles taken from the simulation are shown inset. (**C**) Plots of the distance between the Glu167 and active site zinc over the course of the simulations.

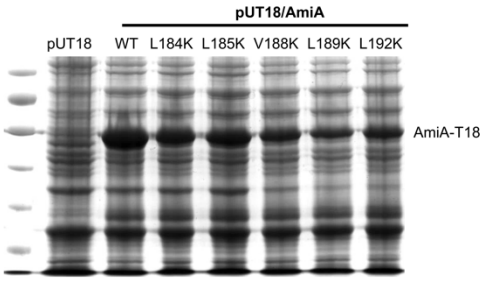

Figure S5: Control experiment showing expression of AmiA variants. The AmiA-T18 fusions used in the bacterial 2-hybrid were expressed in *E. coli* C43 (DE3) and whole cell lysates subjected to SDS PAGE. Lysates from cells carrying the empty pUT18 vector were used as a negative control.

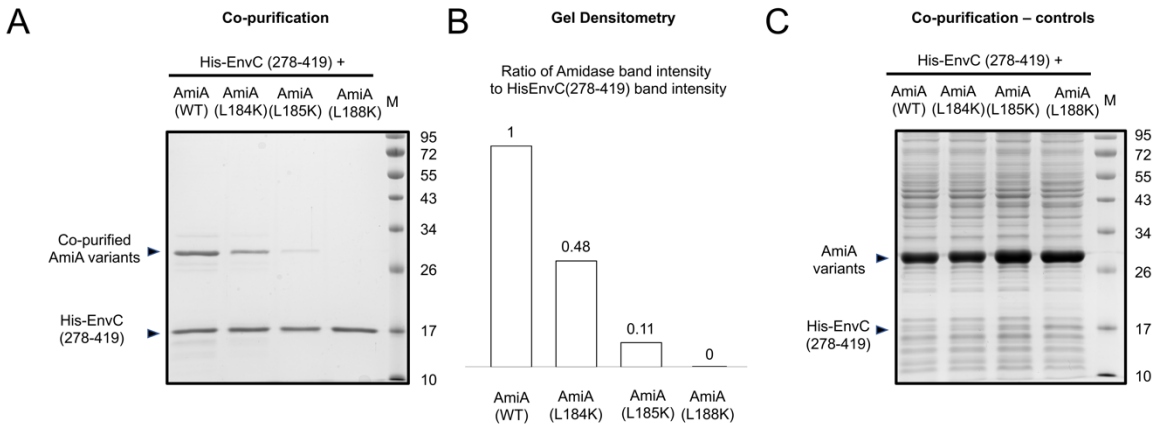

Figure S6: Co-expression and co-purification of AmiA interaction helix variants with the EnvC LytM domain. (A) SDS-PAGE gel showing eluted EnvC-LytM:Amidase complexes after Ni-IMAC purification. Only the EnvC LytM domain is His-tagged, so co-purification of non-tagged amidase variants are dependent on sufficient affinity for the EnvC LytM domain. (B) Gel densitometry of the lefthand gel showing the ratio of amidase band intensity to that of the LytM domain. The ratio of band intensity for the wild type is close to 1:1, while interaction helix variants co-purify with significantly less amidase. There is no sign of an interaction between EnvC LytM and the L188K variant. (C) SDS-PAGE gel showing cleared cell lysates from *E. coli* co-expressing each AmiA variants alongside the His-EnvC LytM domain. These are samples used as input for the Ni-IMAC purification and serve as controls for the expression and stability of the AmiA variants. All the amidases are stably expressed and located at high concentration on the soluble fraction.

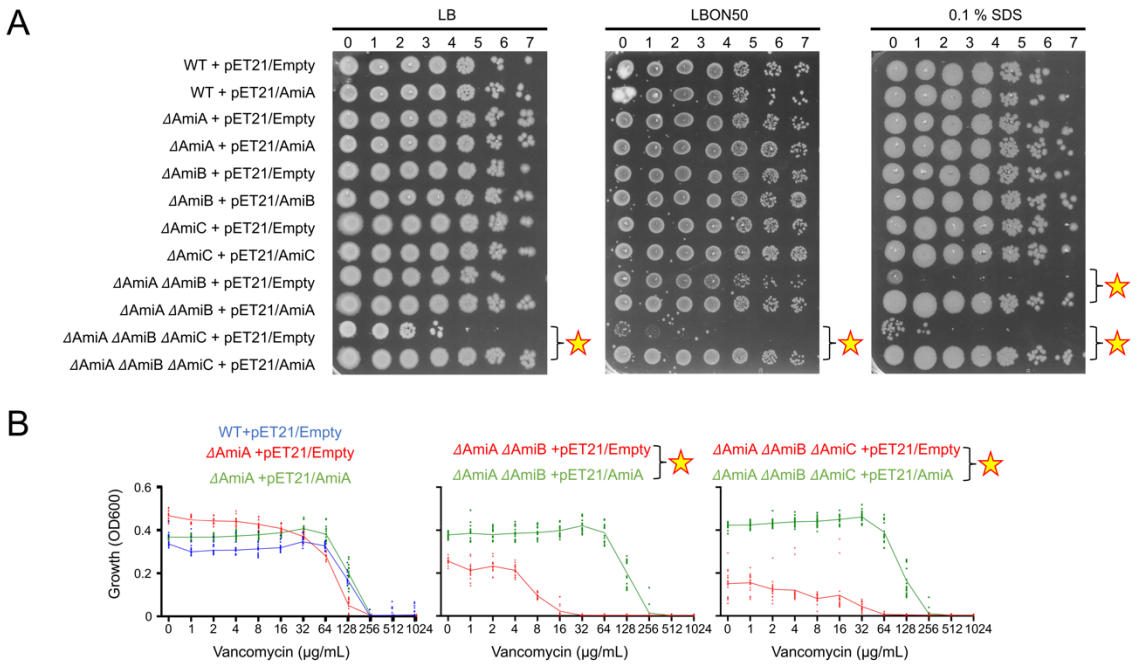

Figure S7: Characterization of cell envelope integrity for single, double and triple amidase deletion strains in a common genetic background. (**A**) Viability of *E. coli* strains with different amidase sets on regular, low salt and high detergent LB agar. WT indicates the wild type (parental) strain, *E. coli* BW25113. Single, double, and triple amidase knockout strains are derived from the parental strain. All strains carry a pET21a based vector (providing ampicillin resistance) which is either empty or carrying the indicated *E. coli* amidase gene. The number of 10-fold serial dilutions from an initial OD 600 1.0 culture is indicated above each agar plate. Stars indicate significant differences in viability between strains complemented by AmiA verses an empty vector. (**B**) Antibiotic susceptibility assays for the wild type strain (BW2511, *left*) and AmiA deletion strain (*Δ*AmiA, *left*), double amidase deletion (*Δ*AmiA *Δ*AmiB, *centre*) and triple amidase deletion (*Δ*AmiA *Δ*AmiB *Δ*AmiC, *right*). Each strain carries either an empty plasmid (pET21a) or AmiA expressing plasmid (pET/AmiA). We find that viability of most single amidase knockouts are similar to the parental strain, but that the uncomplemented triple knockout (*Δ*AmiA *Δ*AmiB *Δ*AmiC +pET21/Empty) shows reduced viability, osmotic sensitivity and susceptibility to SDS and vancomycin (an antibiotic that would not usually pass the outer membrane barrier in *E. coli*). Remarkably, these phenotypes can be almost completely reversed by modest expression of AmiA from a plasmid (*Δ*AmiA *Δ*AmiB *Δ*AmiC +pET21/AmiA).

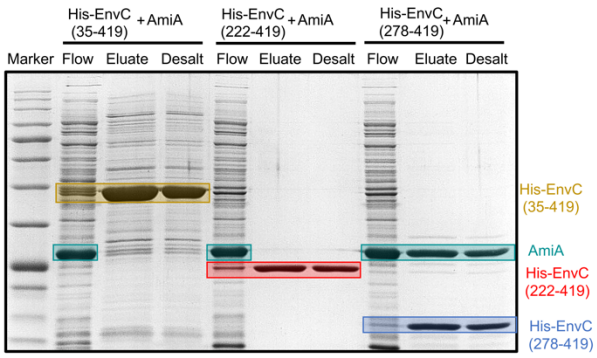

Figure S8: Co-expression and purification experiments for AmiA and three EnvC variants. SDS-PAGE gel showing fractions from three Ni-IMAC purifications. Co-expressed AmiA and His-tagged EnvC variants are indicated above the gel. Samples from the column Flowthrough, a high-imidazole Elution, and a sample taken after removing the imidazole using desalting column are shown for each purification. Untagged AmiA is visible in the flow through of all three experiments, showing it is co-expressed in each case. Co-purification of AmiA was only observed for the His-tagged EnvC-LytM protein.

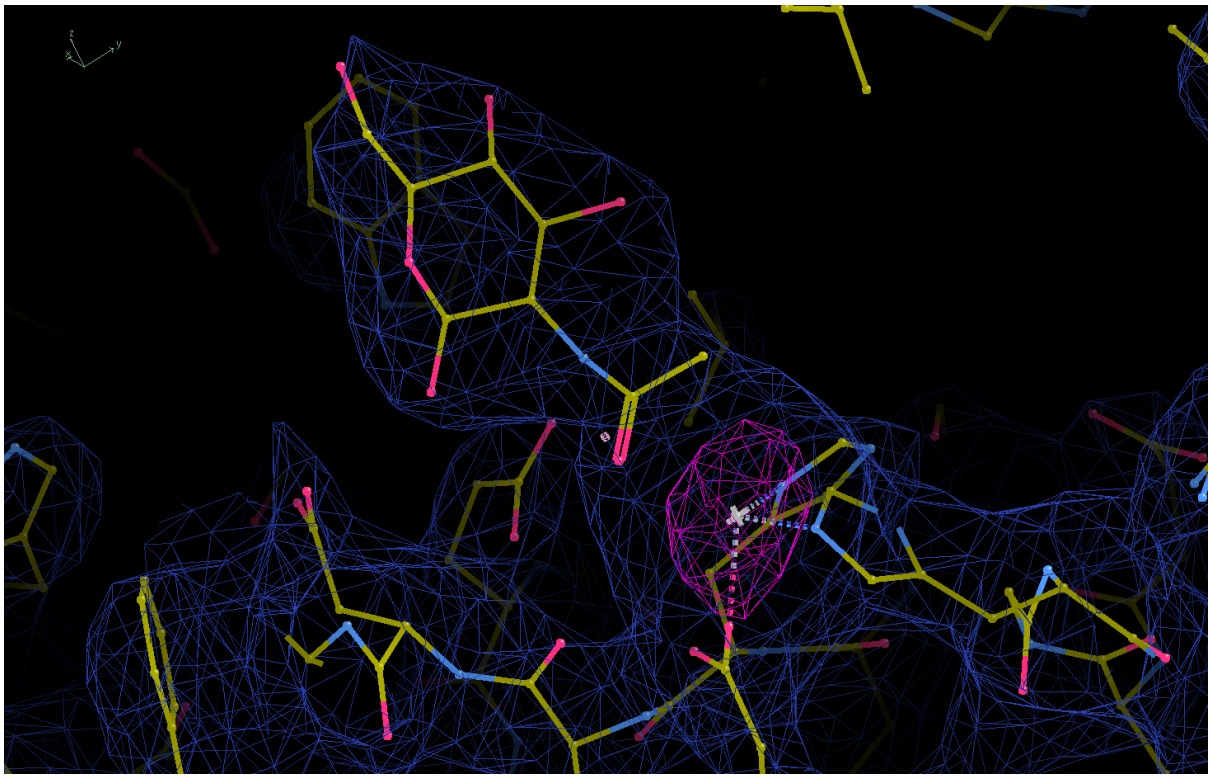

Figure S9: Electron density for an unidentified ligand at the AmiB active site. The standard weighted $2m|F_o|-|F_c|$ map is contoured at 1.25 σ. An anomalous difference map confirming the presence of Zinc is shown in pink, contoured at 5 σ. Figure generated with Coot. Extra electron density opposite the active site zinc most likely indicates the presence of a sugar molecule. A molecule of N-acetyl glucosamine (NAG) is shown built into the residual density. In the deposited coordinates, the sugar is omitted because we have not yet been able to confirm its identity by orthogonal methods. A second monomer of AmiB in the asymmetric unit does not contain the sugar molecule.

Methods

Cloning

All constructs used in this study are listed in **Table S2.** All DNA sequences were confirmed by DNA sequencing (Genewiz). Genes encoding AmiA, AmiB and AmiC were amplified by PCR from *E. coli* DH5α genomic DNA. The products were digested with NdeI and XhoI restriction enzymes and ligated into the similarly digested pET21a. AmiA lacking its signal sequence was generated by PCR and cloned into pET21a via NdeI/XhoI to obtain a C-terminal His tag. This AmiA gene was also ligated into the 3' site of pETDuet-1 via NdeI/XhoI followed by sections of EnvC into the 5' site via BamHI/EcoRI. For bacterial 2-hybrid experiments, AmiA was further subcloned into pUT18C via BamHI/EcoRI.

For co-expression of the amidase-activator, the LytM domain of EnvC (284-420) and the enzymatic domain of AmiB (190-422) from *Citrobacter rodentium* were synthesised by Genscript (with codon optimisation) and engineered into the first and second multiple cloning sites of pETDuet-1 via the BamHI/NotI and NdeI/XhoI sites.

For testing AmiA constructs lacking the regulatory domain, DNA encoding full length AmiA (including an encoded secretion signal) were synthesised by Genscript in pET21a via NdeI/XhoI sites. TB1050 expresses a periplasm-directed AmiA construct in which residues 156-193 (inclusive) were replaced with the amino acid sequence GAA. Tb1055 expresses a periplasm-directed AmiA construct in which residues 152-192 (inclusive) were replaced with the amino acid sequence GSG, and TB1056 expresses a periplasm-directed AmiA construct in which residues 152-192 (inclusive) were removed without replacement.

For site-directed mutagenesis of AmiA, an XbaI/EcoRI fragment encoding the full length AmiA gene was subcloned from pTB1028 into a pUC18 vector and point mutations introduced using the Quikchange Protocol. The mutated genes were subcloned back into pET21a via NdeI/XhoI for expression studies, and also into the Bacterial 2 Hybrid System vectors via the BamHI and EcoRI sites after an intermediate PCR to ensure that the open-reading frame was maintained.

Protein expression and purification

For production of AmiA, plasmid pTB1034 (AmiA with C-terminal His tag) was transformed into *E. coli* C43 (DE3), grown in 2YT at 30 °C to an OD_{600nm} of 0.6 when 1 mM IPTG was

added. After 18 hours further growth, cells were harvested by centrifugation (6,000 x*g*), the cell pellets were resuspended in wash buffer (50 mM HEPES pH 7.2, 300 mM NaCl, 35 mM imidazole) and lysed by 3 passages through an Avestin C3 homogeniser (15,000 psi). The lysate was centrifuged at 30,000 x *g* for 30 min at 6 °C to remove cellular debris and the supernatant loaded onto an immobilised Ni-affinity column pre-equilibrated with the wash buffer. Bound proteins were washed with 25 column volumes of wash buffer before elution in 50 mM HEPES pH 7.2, 300 mM NaCl, 250 mM imidazole. Protein samples were buffer exchanged into 20 mM HEPES pH 7.2, 300 mM NaCl and stored at -80 °C.

For production of the EnvC AmiB complex, N-terminally His-tagged EnvC LytM domain was co-expressed with the enzymatic domain of AmiB from a pETDuet-based plasmid as above, except that the pH of the buffers was maintained at pH 8.0. Purified complexes were then buffer exchanged into 20 mM HEPES pH 8.0, 350 mM NaCl and concentrated to 5.5 mg/ml using a centrifugal filter (Amicon 30 kDa nominal molecular weight cut-off).

Interaction of AmiA with EnvC variants

Co-expression constructs were transformed into *E. coli* C43, grown in 2YT at 30 °C to an OD 600nm of 0.6 when 1 mM IPTG was added. After 18 hours further growth, cells were harvested by centrifugation (6,000 x *g*), the cell pellets were resuspended in wash buffer (50 mM HEPES pH 7.2, 300 mM NaCl, 35 mM imidazole) and lysed using an Avestin C3 homogeniser (15,000 psi). The lysate was centrifuged at 30,000 x *g* for 30 min at 6 °C to remove cellular debris and the supernatant loaded onto an immobilised Ni-affinity column pre-equilibrated with the wash buffer. Bound proteins were washed with 25 column volumes of wash buffer before elution in 50 mM HEPES pH 7.2, 300 mM NaCl, 250 mM imidazole. Excess salt and imidazole was then removed using a PD10 desalting column equilibrated in 20 mM HEPS pH7.2, 150 mM NaCl. For SDS-PAGE analysis, all samples were diluted 10-fold and mixed with a denaturing loading buffer before adding to the gel.

For co-expression and co-purification of AmiA interaction helix variants, experiments were performed as above using expression from pETDuet vectors and co-purification via Ni-IMAC resin. The eluates and cleared lysates were subjected to SDS-PAGE. The quantity of His-tagged LytM domain in the eluate was assessed using gel densitometry with the Biorad Image Lab software and a new gel was run adjusting the volumes loaded so that the amount of LytM domain was similar across lanes. The gel was then further analysed to obtain the band intensity of the LytM domain and any co-purified amidase and a ratio calculated.

Crystallisation

Crystallisation screens were performed using a Formulatrix NT8 crystallisation robot. *E. coli* AmiA was crystallised using a crystallisation reagent composed of (1.4 M tri-sodium citrate and 0.1 M HEPES pH 7.5) and the AmiB-EnvC lytM domain complex (from *Citrobacter rodentium*) was crystallised using (0.8 M Sodium phosphate monobasic monohydrate, 0.8 M Potassium phosphate monobasic, 0.1 M Sodium HEPES, pH 7.5). Both crystallisations used the sitting drop vapour diffusion method with 1 uL drops composed of 666 nL protein solution and 333 nL crystallisation reagent) equilibrated against an 80 µL reservoir of the reagent alone in MRC 2-drop plates. Protein crystals were harvested in litholoops and flash-frozen in liquid nitrogen using standard cryo-crystallography methods.

Structure determination

X-ray diffraction experiments were performed using remote data collection at the Diamond Light Source UK synchrotron. Diffraction images were indexed and integrated using Dials via the synchrotrons data processing pipeline and subsequently scaled inhouse using Aimless (4). Further processing used programs from the CCP4 suite (5). Initial phase determination used the molecular replacement method implemented in Phaser (6). For AmiA, we used an initial structure prediction generated using the Alphafold prediction algorithm (7) as implemented in Colabfold (8). For the amidase-activator complex, we used our experimentally determined model of AmiA and the LytM domain of *E. coli* EnvC extracted from PDB entry 6TPI - a structure of EnvC bound to the periplasmic domains of FtsX (1). Models were completed using alternating rounds of model re-building with Coot (9) and refinement with Refmac (10). Non-crystallographic symmetry restraints were applied in both cases. Refinement of the AmiB-EnvC complex additionally used secondary restraints generated using ProSMART (11). Validation used tools in Procheck (12) and Coot (9) to assess geometry, and Rampage (13) to assess the distribution of backbone angles in the Ramachandran plot. The presence of zinc was confirmed using X-ray fluorescence and calculation of anomalous difference maps. Coordinates and structure factors have been deposited at the protein data bank.

Construction of amidase knockout strains

Single knockout *E. coli* strains lacking *amiA* and *amiB* were taken directly from the Keio collection. These strains are both derivatives of the parent strain, *E. coli* BW25113, and have a kanamycin cassette on the chromosome in place of the amidase-encoding gene (BW25113 *ΔamiA::Kan* and BW25113 *ΔamiB::Kan*). The *amiAB* double knockout (BW25113 *ΔamiA*

⊿amiB::Kan) was constructed by removing the kanamycin cassette from the BW25113*⊿amiA::Kan* strain using FLP-FRT recombination, and then using lambda red recombination (14) (as implemented in the Genebridges gene deletion kit) to re-insert a kanamycin cassette into the *amiB* gene. The triple deletion was constructed similarly, by first removing the kanamycin cassette from the BW25113 *⊿amiA ⊿amiB::Kan* double knockout strain, and then re-inserting a kanamycin resistance cassette into the *amiC* gene. All strains were checked for kanamycin resistance and verified using PCR amplification of the three gene sites using primers on either side of each genetic locus.

E. coli viability assays on agar plates

E. coli strain BW25113, variations of this parental strain with different genes 'knocked out' and the C43 strain were transformed with plasmids carrying either the wild type AmiA, AmiB, AmiC or variant AmiA. Cells were grown in LB supplemented with 50 µg/ml ampicillin to OD_{600} = 1.0. Each culture was 10-fold serially diluted in LB supplemented with 50 µg/ml ampicillin and 1 mM IPTG. 3 µl of each dilution was spotted onto LB agar containing 50 µg/ml ampicillin, 1 mM IPTG and with/without 0.1% SDS. Culture was also spotted onto LBON50 agar (LB with no salt, diluted 2-fold with water) with 50 µg/ml ampicillin and 1 mM IPTG. Plates were incubated overnight at 37 °C and then imaged using an Epson scanner. Images were uniformly contrast-adjusted and converted to greyscale.

Vancomycin MIC determination

Minimum inhibitory concentrations were determined in LB supplemented with 50 µg/ml ampicillin and 1 mM IPTG. Each set of vancomycin concentrations was generated by 2-fold serial dilutions. Experiments were conducted in 96-well plates with a final volume of 200 µl in each well, all of which were seeded with 5 µl of starter culture that was preadjusted to OD_{600} = 0.01 by dilution of seed cultures that were grown to between 0.6 and 1.0 (OD_{600}). After 18 hours of growth at 37 °C, plates were read in a MultiSkan Sky plate reader (Thermo Scientific) using the absorbance at 600 nm wavelength. MICs are presented as the median of several determinations (typically, twenty-four MIC measurements consisting of three biological repeats with eight technical repeats for each).

Bacterial 2-hybrid protein-protein interaction studies

The Bacterial Adenylate Cyclase Two Hybrid (BACTH) system was used to perform bacterial 2-hybrid experiments (15). 2 ng of each of two complimentary plasmids were co-transformed into *E. coli* BTH101 cells and grown overnight at 30 °C in LB (50 µg/ml ampicillin, 25 µg/ml kanamycin). 5 µl was spotted onto LB agar plates containing 50 µg/ml ampicillin, 25 µg/ml kanamycin, 40 µg/ml X-gal and 0.5 mM IPTG and grown at 20 °C for ~64 hr. The negative control was a pair of empty pUT18 and pKT25 vectors. The positive control was a pair of plasmids containing a leucine zipper which dimerises. The presence of blue colonies indicated that the expressed proteins had interacted.

Phase Contrast Microscopy

Triple knockout *E. coli* ΔAmiABC cells carrying pET21a-based plasmids encoding AmiA variants were grown overnight in LB supplemented with 50 µg/ml ampicillin and 1mM IPTG at 37 °C. A sample of each was diluted with LB and spotted onto an agarose-coated glass slide for immediate observation. Images were collected using a Leica Microsystems Model TL LED microscope.

Molecular Dynamics Simulations

All simulations were performed using Gromacs 2021 using the charmm36m forcefield (16, 17). Simulated proteins were appropriately protonated, centred, and solvated with TIP3P water in a rhombic dodecahedron box with 0.15 M NaCl. Systems were energy minimized using a steepest descent algorithm to 1000 kJ mol^{-1} nm^{-1} before equilibration for 1 ns with 1000 x 1000 x 1000 kJ mol^{-1} nm^{2} position restraints on all protein atoms (excluding hydrogens). Post equilibration, five production repeats were generated and simulated unrestrained for 500 ns, each with different starting velocities. A 2 fs timestep was applied to an NPT ensemble with either an isotropic C-rescale barostat for production simulations or an isotropic Berendesen barostat for equilibration simulations at 1 bar and V-rescale temperature coupling where protein and solvent were individually coupled (18–20). Electrostatic terms were described using PME with a cut-off of 1.2 nm while van der Waals interactions were shifted between 1 and 1.2 nm. Hydrogen bonds were constrained with LINCS (21) and SETTLE (22) was used to constrain the water bond angles and distances. Analysis was performed using Gromacs and MDAnalysis (23). PyMOL was used for visualisation (24).

Supplemental References

1. J. Cook, *et al.*, Insights into bacterial cell division from a structure of EnvC bound to the FtsX periplasmic domain. *Proc. Natl. Acad. Sci. U.S.A.* **117**, 28355–28365 (2020).

2. D. C. Yang, K. Tan, A. Joachimiak, T. G. Bernhardt, A conformational switch controls cell wall-remodelling enzymes required for bacterial cell division: Control of cell wall-remodelling enzymes. *Molecular Microbiology* **85**, 768–781 (2012).

3. M. Rocaboy, *et al.*, The crystal structure of the cell division amidase AmiC reveals the fold of the AMIN domain, a new peptidoglycan binding domain: Crystal structure of AmiC of *Escherichia coli*. *Molecular Microbiology*, n/a-n/a (2013).

4. P. R. Evans, G. N. Murshudov, How good are my data and what is the resolution? *Acta Crystallogr D Biol Crystallogr* **69**, 1204–1214 (2013).

5. M. D. Winn, *et al.*, Overview of the *CCP* 4 suite and current developments. *Acta Crystallogr D Biol Crystallogr* **67**, 235–242 (2011).

6. A. J. McCoy, *et al.*, *Phaser* crystallographic software. *J Appl Crystallogr* **40**, 658–674 (2007).

7. J. Jumper, *et al.*, Highly accurate protein structure prediction with AlphaFold. *Nature* **596**, 583–589 (2021).

8. M. Mirdita, *et al.*, ColabFold: making protein folding accessible to all. *Nat Methods* **19**, 679–682 (2022).

9. P. Emsley, B. Lohkamp, W. G. Scott, K. Cowtan, Features and development of *Coot*. *Acta Crystallogr D Biol Crystallogr* **66**, 486–501 (2010).

10. G. N. Murshudov, *et al.*, *REFMAC* 5 for the refinement of macromolecular crystal structures. *Acta Crystallogr D Biol Crystallogr* **67**, 355–367 (2011).

11. R. A. Nicholls, M. Fischer, S. McNicholas, G. N. Murshudov, Conformation-independent structural comparison of macromolecules with *ProSMART*. *Acta Crystallogr D Biol Crystallogr* **70**, 2487–2499 (2014).

12. R. A. Laskowski, M. W. MacArthur, D. S. Moss, J. M. Thornton, PROCHECK: a program to check the stereochemical quality of protein structures. *J Appl Crystallogr* **26**, 283–291 (1993).

13. S. C. Lovell, *et al.*, Structure validation by Cα geometry: ϕ,ψ and Cβ deviation. *Proteins* **50**, 437–450 (2003).

14. Y. Zhang, F. Buchholz, J. P. P. Muyrers, A. F. Stewart, A new logic for DNA engineering using recombination in Escherichia coli. *Nat Genet* **20**, 123–128 (1998).

15. G. Karimova, J. Pidoux, A. Ullmann, D. Ladant, A bacterial two-hybrid system based on a reconstituted signal transduction pathway. *Proc. Natl. Acad. Sci. U.S.A.* **95**, 5752–5756 (1998).

16. M. J. Abraham, *et al.*, GROMACS: High performance molecular simulations through multi-level parallelism from laptops to supercomputers. *SoftwareX* **1–2**, 19–25 (2015).

17. J. Huang, *et al.*, CHARMM36m: an improved force field for folded and intrinsically disordered proteins. *Nat Methods* **14**, 71–73 (2017).

18. M. Bernetti, G. Bussi, Pressure control using stochastic cell rescaling. *J. Chem. Phys.* **153**, 114107 (2020).

19. G. Bussi, D. Donadio, M. Parrinello, Canonical sampling through velocity rescaling. *The Journal of Chemical Physics* **126**, 014101 (2007).

20. H. J. C. Berendsen, J. P. M. Postma, W. F. van Gunsteren, A. DiNola, J. R. Haak, Molecular dynamics with coupling to an external bath. *The Journal of Chemical Physics* **81**, 3684–3690 (1984).

21. B. Hess, H. Bekker, H. J. C. Berendsen, J. G. E. M. Fraaije, LINCS: A linear constraint solver for molecular simulations. *J. Comput. Chem.* **18**, 1463–1472 (1997).

22. S. Miyamoto, P. A. Kollman, Settle: An analytical version of the SHAKE and RATTLE algorithm for rigid water models. *J. Comput. Chem.* **13**, 952–962 (1992).

23. N. Michaud-Agrawal, E. J. Denning, T. B. Woolf, O. Beckstein, MDAnalysis: A toolkit for the analysis of molecular dynamics simulations. *J. Comput. Chem.* **32**, 2319–2327 (2011).

24. Schrödinger, LLC, The PyMOL Molecular Graphics System, Version 1.8 (2015).